Active site identification and modification of electronic states by atomic-scale doping to enhance oxide catalyst innovation

Ying Xin,[†] Nana Zhang,[†] Qian Li,[†] Zhaoliang Zhang,*[,†] Xiaoming Cao,*[,‡] Lirong Zheng,[§]

Yuewu Zeng,[∥] James A. Anderson*[,⊥]

[†]School of Chemistry and Chemical Engineering, Shandong Provincial Key Laboratory of Fluorine Chemistry and Chemical Materials, University of Jinan, Jinan 250022, China

[‡]Center for Computational Chemistry, School of Chemistry and Molecular Engineering, East China University of Science and Technology, Shanghai 200237, China

[§]Institute of High Energy Physics, Chinese Academy of Sciences, Beijing 100049, China

[∥]Center of Electron Microscopy and State Key Laboratory of Silicon Materials, Zhejiang University, Hangzhou 310027, China

[⊥]Surface Chemistry and Catalysis Group, Materials and Chemical Engineering, University of Aberdeen, AB24 3UE, United Kingdom

ABSTRACT: Identification of the catalytic active site is critical in the designing and developing of advanced heterogeneous catalysts. Many high-precision experimental techniques, as well as computational methods, have been developed to address this problem, but identifying the active site for composite oxide catalysts still remains a challenging task due to their complexity and indiscernible microstructures. Herein, we provide a key new insight into the active site within a composite oxide catalyst by investigating an iron-based oxide catalyst with complex components. The dopant atoms with octahedral coordination located at substitution-sites in the Fe_2O_3 lattice, tune the electronic structure of the adjacent iron atoms, which act as the active sites which lead to enhanced catalytic activity. This atomic-scale doping is different from the emerging single-atom catalyst concept, in which the single atom on the support is the active site, and which provide an alternative methodology of improving the activity of heterogeneous catalysts with maximized heteroatom efficiency.

1. INTRODUCTION

Based on the different complexity levels, heterogeneous solid catalysts in multicomponent systems can be divided into three typologies: i) single-site heterogeneous catalysts; ii) supported metal catalysts; iii) transition metal oxide catalysts.[1] However, the elucidation and understanding of structure-function relationships is a long-standing challenge in the field of heterogeneous catalysis, despite significant ongoing research in the area. As a landmark contribution to catalyst theory, Taylor suggested that a catalysed chemical reaction occurs at a limited number of "active

48 sites," irrespective of the type of heterogeneous catalyst.[2] This finding initiated a worldwide

49 research surge to explore the nature of these active sites. Progress however is often hampered by

50 the difficulty of identifying the active site within a complex matrix on a catalyst surface.[3-5] The

51 different types of heterogeneous catalysts commonly exhibit a variety of different surface sites

52 that are difficult to identify and quantify. The scenario is further complicated when multiple sites

53 work together in turning over a reaction.[3] In particular, for transition metal oxide catalysts, the

54 heteroatoms or ions are often intentionally incorporated into the host lattices to control and

55 manipulate their properties and morphology changes, ultimately in order to improve their

56 functional performance.[6-10] The substitution of dopant atoms in host oxides conventionally

57 results in the formation of composite oxides, containing multiple phases, solid solutions, or even

58 amorphous species.[11-13] Due to their complexity and indiscernible microstructures, the active

59 sites have not been clearly and systematically investigated, especially for poorly-crystallinity or

60 amorphous samples. Hence, it is difficult to pick out the catalytic active site from an assembly of

61 potential candidates in a composite oxide catalyst, and the detailed structure of active sites as

62 well as the functional mechanism still remains elusive, and requires further exploration.[14]

63   On the basis of the previous studies, the dopant in composite oxides are assumed to disrupt the

64 chemical bonding at the surface of the host oxide, and the active sites are ascribed to either the

65 oxygen anions near the dopant or the dopant itself.[8,15-18] Here, novel insight into the catalytic

66 active site of a composite oxide catalyst is presented using an iron-based oxide with complex

67 components as an example. The atomic-resolution and visualized characterization combined with

68 the computer simulations accurately identify the active sites in Fe_2O_3-based oxide catalyst, and

69 uncover the reason for the enhanced activity, as exemplified by the selective catalytic reduction

70 (SCR) of NO_x. The dopant atoms with octahedral coordination located at substitution-sites of the

3

81 Fe_2O_3 lattice tune the electronic structure of surface Fe atoms, which then acts as the effective

82 active sites. This opens up a different perspective on active sites of composite oxide catalysts

83 from the emerging single-atom (ion) catalysis concept, in which the single atom or ion on the

84 support is the active site, and thus provides an alternative route to improving the activity of

85 heterogeneous catalysts which maximises heteroatom efficiency by atomic-scale doping.[19]

86

2. EXPERIMENTAL SECTION

88 The Mo_x-Fe_2O_3 and W_y-Fe_2O_3 samples (x represents Mo/Fe atomic ratio, and y represents

89 W/Fe atomic ratio from ICP data) were prepared by a co-precipitation method using an aqueous

90 solution of ammonium molybdate (($NH_4)_6Mo_7O_{24}·4H_2O$, 200 mL. The pH value was adjusted to

91 9.0 by ammonium hydroxide with stirring for 30 min)/sodium tungstate ($Na_2WO_4·2H_2O$, 200

92 mL) and ferrous sulfate ($FeSO_4·7H_2O$, 100 mL) with ammonium hydroxide ($NH_3·H_2O$, 25-28

93 wt.%) at 35 °C, with the pH value of the precipitation process controlled at above 6.0 and that of

94 the resulting solution maintained at 9.0. The total amount of the metallic salt precursor was 0.03

95 mol. Ascorbic acid ($C_6H_8O_6$, 100 mg) was added to the initial iron precursor solution to promote

96 the reducibility of the Fe^{2+}. The obtained slurry was aged with stirring at 35°C for three hours

97 and subsequently filtrated and washed. The resulting solid was dried overnight at 70°C and

98 calcined at 500°C for 5 h. For comparison and further investigation, Fe_2O_3, MoO_3, and

99 $Fe_2(MoO_4)_3$ were also prepared. More experimental details are described in the Supporting

100 Information.

3. RESULTS AND DISCUSSION

4
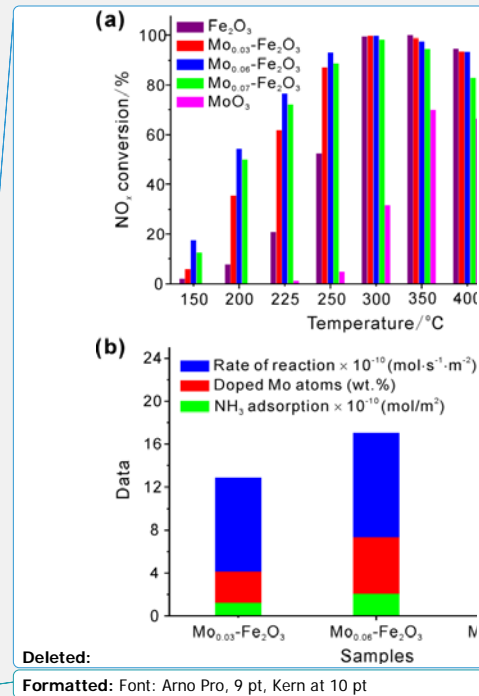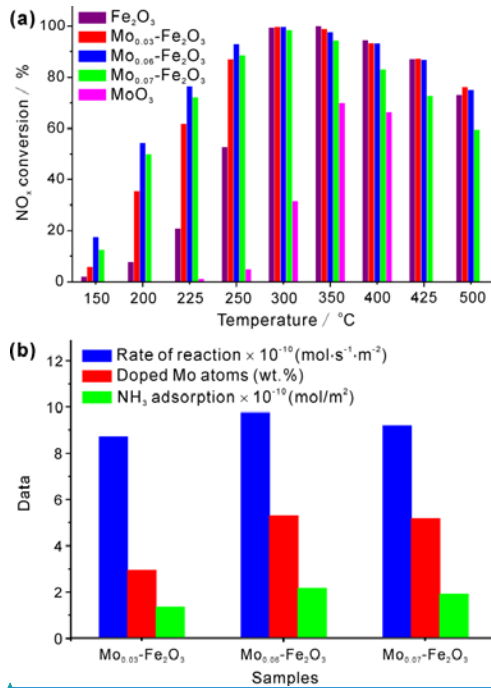
Figure 1. (a) NO$_x$ conversion over Mo$_x$-Fe$_2$O$_3$ catalysts in SCR reactions as a function of reaction temperature, (b) SCR reaction rates, quantities of Mo dopant atoms, and NH$_3$ adsorption on Mo$_x$-Fe$_2$O$_3$ catalysts.

As a critically important heterogeneous catalyst, Fe$_2$O$_3$-based oxide catalysts have been widely investigated due to their inherently environmentally benign character, excellent redox properties, and the prominent thermal stability.[20-24] In this work, a series of Mo doped Fe$_2$O$_3$ composite catalysts with different Mo content were prepared *via* a modified co-precipitation method, followed by calcination at 500°C (see Supporting Information). The catalysts obtained were designated as Mo$_x$-Fe$_2$O$_3$, in which "x" represents the mole ratio of Mo/Fe (ICP data, Table S1).

Deleted:

Formatted: Font: Arno Pro, 9 pt, Kern at 10 pt

Deleted: Mo$_a$

Deleted: amounts

Deleted: Mo

Deleted: f

Deleted: Mo$_a$

Deleted: because of

Deleted: the

Deleted: ty

Deleted:

Deleted: Mo$_a$

Deleted: a

139 The weak XRD peaks of Mo_x-Fe_2O_3 are indexed as a hematite phase of Fe_2O_3 (JCPDS 33-0664),

140 while no diffraction peaks due to Mo-containing species were detected (Figure S1a). The slightly

141 decreased lattice parameters (*a*) of Fe_2O_3 phase linearly correlate with the increasing Mo content

142 in Mo_x-Fe_2O_3, suggesting that the dopant Mo atoms give rise to the lattice contraction of the

143 Fe_2O_3 crystalline, owing to the smaller ionic radius of Mo^{6+} (six-fold coordination, 0.59 Å)

144 compared with Fe^{3+} (six-fold coordination, 0.645 Å) (Figure S1b and Table S1). To verify the

145 effect of dopant Mo atoms on the catalytic performance of Mo_x-Fe_2O_3 catalysts, SCR was set as

146 a representative reaction. Consequently, the excellent redox property of Fe_2O_3 is potentially

147 integrated with the promoting effect of dopant Mo atoms, fabricating a novel and improved

148 catalyst compared to the existing ones.[22,23,25-28] As expected, the SCR performances of Mo_x-

149 Fe_2O_3 are superior to those of the pure oxides, which additionally provide an extended active

150 temperature window (temperatures at which >90% NO_x conversion was achieved) especially at

151 low temperature (Figures 1a and S2).

152   The nature of Mo dopant atoms and their impact on the structure and properties of Mo_x-Fe_2O_3

153 were investigated in great detail. The geometry and morphology of Mo_x-Fe_2O_3 were greatly

154 affected by the dopant Mo atoms (Figure S3). The low-resolution HAADF image and

155 corresponding EDS elemental mappings of $Mo_{0.06}$-Fe_2O_3 proved that the dopant Mo atoms, and

156 Fe and O are highly dispersed throughout the whole region of aggregates without forming larger

157 bulk Mo-containing oxides (Figure 2a). The corresponding HRTEM image (Figure 2b) exhibit

158 clear lattice fringes which are ascribed to the (104) crystal plane of Fe_2O_3 (labeled by white

159 lines), meanwhile a few lattice spacings (labeled by yellow lines) correspond to the crystal

160 planes of monoclinic $Fe_2(MoO_4)_3$ phase. In view of lack of sensitivity of X-ray diffraction to

161 small clusters or low-concentration phases, the $Fe_2(MoO_4)_3$ phase was not detected in XRD

Deleted: Mo_a

Deleted: Mo_a

Deleted: Mo_a

Deleted: Mo_a

Deleted: In general, $Mo_{0.06}$-Fe_2O_3 possessed not only the optimal activity but also good resistance to H_2O and SO_2 (Figure S3).

Deleted: detailed information

Deleted: Mo

Deleted: Mo_a

Deleted: Mo_a

Deleted: profoundly

Deleted: S4

174 patterns of Mo_x-Fe$_2$O$_3$ (Figure S1a). Considering the low activity of Fe$_2$O$_3$, the improved activity

175 of Mo_x-Fe$_2$O$_3$ may be ascribed to the presence of Fe$_2$(MoO$_4$)$_3$ microcrystals or the synergistic

176 effect of Fe$_2$O$_3$ and the Fe$_2$(MoO$_4$)$_3$ microcrystals. However, this proposal is rejected because of

177 the poor SCR activities of pure Fe$_2$(MoO$_4$)$_3$ and mechanically mixed catalysts containing Fe$_2$O$_3$

178 and Fe$_2$(MoO$_4$)$_3$ (Figures S4 and S5). At this point, the active species, which are responsible for
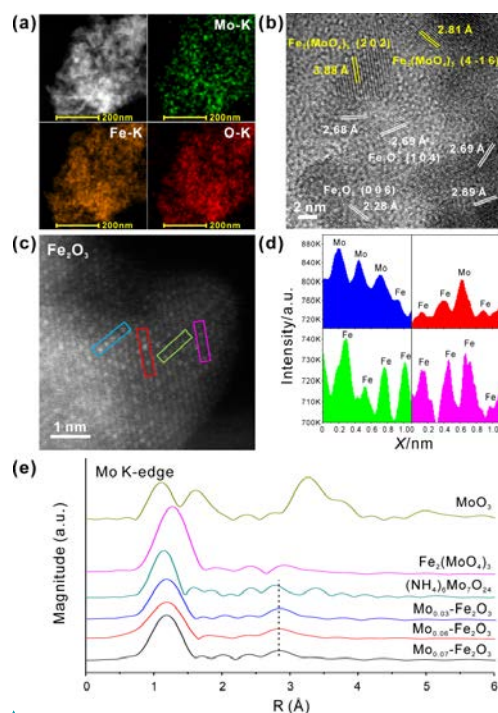
179 the improved activity, are unclear.

180

183 **Figure 2.** (a) HAADF images and EDS elemental mappings, (b) HRTEM image of Mo$_{0.06}$-

184 Fe$_2$O$_3$, (c) aberration-corrected HAADF-STEM image from a two-dimensional lattice of Fe$_2$O$_3$

7
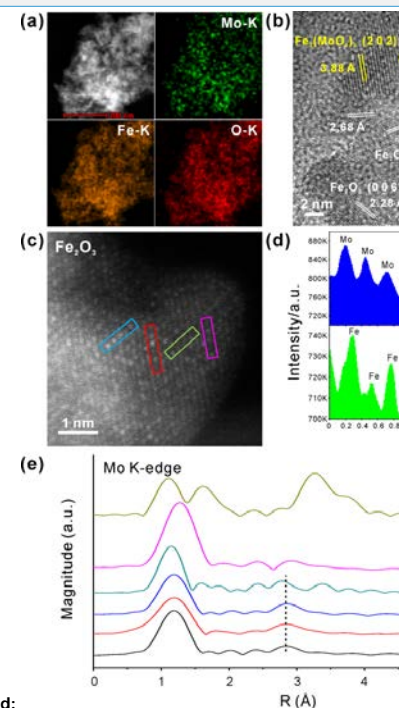
190 microcrystal (the blue and red rectangles indicate the single or poly-molybendum species with

191 several Mo atoms linked by oxygen bridging bonds; the green and pink shapes indicate several

192 Fe atoms linked by oxygen bridging bonds), (d) line intensity profile across Mo and Fe atoms as

193 indicated in (c), and (e) the radial structure function (RSF) curves of Mo K-edge XAFS spectra

194 for Mo_x-Fe_2O_3 catalysts and the reference samples. The dashed line indicates the Mo-Mo shell.

195

196 X-ray photoelectron spectroscopy (XPS) was used to characterize the surfaces of Mo_x-Fe_2O_3.

197 The spectra of Fe 2p for Fe_2O_3 and Mo_x-Fe_2O_3 catalysts showed that no obvious change in

198 binding energies was observed after the doping of Mo due to the excess Fe_2O_3 in Mo_x-Fe_2O_3

199 catalysts (Figure S6a). Nevertheless, compared with MoO_3, the binding energies of Mo 3d for

200 Mo_x-Fe_2O_3 and $Fe_2(MoO_4)_3$ showed an obvious shift towards lower binding energies due to the

201 strong interaction between Mo and Fe species (Figure S6b).[29,30] The O 1s peaks can be fitted

202 using two peaks, referred to as the lattice oxygen at ~530.4 eV (O_β) and the chemisorbed surface

203 oxygen at ~531.6 eV (O_α) (Figure S6c).[30] The surface atomic ratios of Mo/Fe obtained from XPS

204 data are much higher than those of the bulk (ICP data, Table S1), suggesting enrichment by Mo

205 at the surface of Mo_x-Fe_2O_3.

206 The atomic resolution high-angle annular dark field (HAADF) scanning transmission electron

207 microscopy (STEM) was used to provide directly interpretable images of surface Mo species.[16]

208 The arrangement of Fe and/or Mo atoms is uniform in the $Fe_2(MoO_4)_3$ microcrystal (Figure S7a).

209 In contrast, besides the uniform arrangement of Fe atoms, several bright flecks were detected in

210 the Fe_2O_3 crystallites, which are ascribed to isolated Mo atoms due to the difference in Z

211 contrasts between Fe and Mo atoms (Figures 2c and S7b). Although the oxygen atoms are not

8

228 resolved by HAADF imaging, the Mo species in this sample are known to be fully oxidized after

229 the high-temperature calcination stage. Therefore, Mo atoms coordinated with O atoms are

230 doped into the Fe_2O_3 lattice. Furthermore, HAADF intensity variations existed within the two-

231 dimensional lattice of Fe_2O_3 crystallites according to the line intensity profiles (Figures 2c and

232 d). As shown in Figure 2d, the adjacent Mo atoms (blue rectangle) show a similar level of

233 intensity as an isolated Mo atom (red rectangle). Due to the lower atomic mass compared to Mo

234 atoms, the Fe atoms in proximity of Mo atoms clearly show lower intensity, similar to those in

235 the pure Fe_2O_3.[16] More importantly, all of the Mo atoms with a high contrast occupy the lattice

236 sites, confirming that these Mo atoms are doped into the Fe_2O_3 lattice matrix.[31]

237   X-ray absorption fine structure (XAFS) spectra for Mo_x-Fe_2O_3 were measured to obtain

238 detailed structural information of dopant Mo atoms in the bulk structure.[16,32] The Fe K-edge

239 XANES spectra and RSF curves for Fe_2O_3 and Mo_x-Fe_2O_3 are similar, indicating that the Fe

240 atoms in Mo_x-Fe_2O_3 are trivalent and occupy octahedral (O_h) coordination similar to Fe_2O_3

241 (Figure S8). In the case of the Mo K-edge, the peak position and shape of the normalized

242 XANES and RSF curves for Mo_x-Fe_2O_3 corresponded well with those of $(NH_4)_6Mo_7O_{24}$, which

243 implies that most of the hexavalent Mo atoms in Mo_x-Fe_2O_3 exist in the same O_h coordination

244 environment as that of the $(Mo_7O_{24})^{6-}$ anions (Figures 2e and S9a).[33] However, the Mo atoms in

245 $Fe_2(MoO_4)_3$ crystals are in tetrahedral (T_d) coordination as indicated by its different XANES

246 spectrum.[34] According to the above results, it may be deduced that Fe atoms in Fe_2O_3 lattice are

247 substituted by Mo atoms, which are in the same O_h coordination as Fe atoms in the Fe_2O_3 lattice.

248 The majority of the Mo-containing species in Mo_x-Fe_2O_3 are Mo atoms which substitute for Fe

249 atoms in the Fe_2O_3 lattice with O_h coordination. The relative amount of dopant Mo atoms with

250 O_h coordination, i.e. the $(Mo_7O_{24})^{6-}$ species, obtained from the XAFS spectra using linear

Deleted: Hence,

Deleted: clearly

Deleted: Mo_a

Deleted: Mo_a

Deleted: Mo_a
Deleted: in

Deleted: S9

Deleted: Mo_a

Deleted: Mo_a

Deleted: S10a

Deleted: Above all, t
Deleted: Mo_a

263   combination fitting (LCF) (Figures S9b-d) has the same tendency with the normalized rate

264   expressed on the basis of the BET surface area (r_{BET}) (Figure 1b).[35] This provides convincing

265   evidence that the dopant Mo atoms with O_h coordination contribute to the promoting of activity.

266   To further clarify how the chemical properties of Mo_x-Fe_2O_3 were improved by the dopant Mo

267   atoms, the redox properties and acidity were assessed as these are believed to be crucial

268   characteristics associated with SCR.[26,36-38] Surprisingly, neither the redox properties (H_2-TPR,

269   Figure S10a) nor the NO oxidation performance (Figure S10b) of Mo_x-Fe_2O_3 were promoted by

270   doping with Mo atoms. The acidity of Mo_x-Fe_2O_3 was examined by temperature-programmed

271   desorption of NH_3 (NH_3-TPD) (Figure S11). In comparison with Fe_2O_3, a greater amount of

272   ammonia was desorbed in the range 100-500°C (NH_3 adsorption on MoO_3 was negligible),

273   indicating enhanced acidity of Mo_x-Fe_2O_3. By integrating the NH_3-TPD peak areas, the relative

274   amounts of adsorbed NH_3 may be correlated with the reaction rate of Mo_x-Fe_2O_3 (Figure 1b),

275   indicating that promotion of activity can be primarily ascribed to the enhanced acidity, resulting

276   from the doping by Mo atoms in Fe_2O_3.

277   The improvement arising from acidity modification was further assessed by *in situ* FTIR of

278   NH_3 adsorption and SCR reactions (Figures S12 and S13). Only Brønsted acid sites were

279   detected for Fe_2O_3, while both Lewis acidic and Brønsted acidic sites were observed for $Mo_{0.06}$-

280   Fe_2O_3 (Figure S13).[39-44] The additional Lewis acid sites are believed to be associated with the

281   doping of Mo atoms in Fe_2O_3. Furthermore, a band at ~1328 cm^{-1} detected for $Mo_{0.06}$-Fe_2O_3, may

282   be attributed to an additional surface species resulting from the combination of adsorbed and

283   activated NH_3 at Lewis acid sites and NO_x (Figure S13).[40,42] Both observations strongly suggest

284   that the presence of Lewis acid sites created by the doping of Mo in Mo_x-Fe_2O_3 are responsible
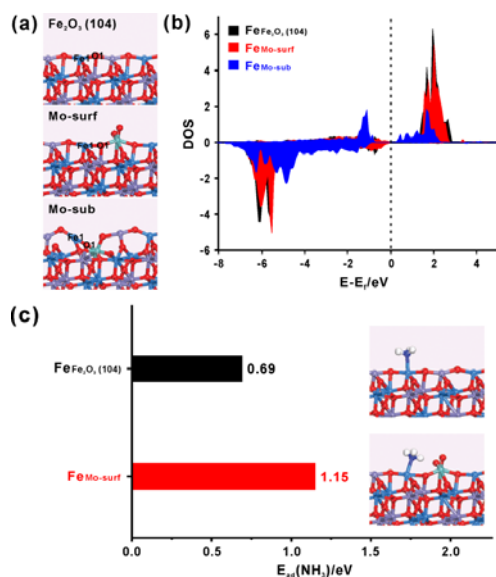
308   for the improved SCR activity. A question remains as to whether the Lewis acid site is associated

309   directly with these dopant Mo atoms?

310

311

312   **Figure 3.** (a) The optimized surfaces of pure Fe_2O_3 (104), Mo-doped Fe_2O_3 (104) at surface

313   (denoted as Mo-surf), and subsurface Mo-doped Fe_2O_3 (104) (denoted as Mo-sub) models; (b)

314   the local density of states of 3d orbitals of Fe1, and (c) adsorption configurations and adsorption

315   energies of NH_3 on Fe sites of Fe_2O_3 (104), and Mo-surf. The center of valence d-band of Fe1 at

316   Fe_2O_3 (104), Mo-surf and Mo-sub are located at -4.82, -4.76 and -4.32 eV, respectively. The

317   center of conduct d-band of Fe1 at Fe_2O_3 (104), Mo-surf and Mo-sub are located at 2.05, 2.04

318   and 1.54 eV, respectively. The purple, blue, cyan, and red balls, respectively, represent Fe with

319   up spin, Fe with down spin, Mo, and O atoms.

320

In order to elucidate the nature of the enhanced Lewis acidity, DFT calculations were performed using the Vienna ab-initio simulation package.[45,46] The antiferromagnetic hematite (α-Fe_2O_3) which is the thermodynamically most stable phase of iron oxide was investigated (Figure S14). As displayed in TEM images (Figure 2), the (104) surface was exposed. DFT calculations were performed on the pure and Mo-doped Fe_2O_3 (104). The doped Mo is energetically most likely to occupy the surface Fe site with broken O_h coordination, which is 0.95 eV more stable than the second most stable subsurface Fe site with O_h coordination (Figure 3a). Additionally, once the Mo is doped into the surface, the dissociative adsorption of O_2 is facilitated at the Mo site (Figure S15), which is shown by the relative concentration ratios of surface adsorbed oxygen ($O_\alpha/(O_\alpha+O_\beta)$) which correlates with the amount of dopant Mo atoms and reaction rates (Figure 1b, and Table S1). After the dissociative adsorption of O_2, this surface dopant Mo will form an O_h coordination site as well, consistent with XAFS results.

By integrating the contribution of the energy bands up to the Fermi level based on the projected Crystal Orbital Hamilton Population (IpCOHP) analysis,[47,48] the IpCOHP values between the dopant Mo and O1 (-4.43 eV and -7.44 eV, corresponding to the Mo doped at the surface and subsurface sites, respectively) are found to be more negative than those of Fe1 and surface O1 connecting with Mo and Fe1 (-1.83 eV and -0.05 eV, corresponding to the Mo doped at the surface and subsurface sites, respectively). This suggests strong bonding between Mo and O1 which is ascribed to the strong oxophilicity of Mo, as indicated above. Compared with the IpCOHP value between surface neighboring Fe1 and O1 in the pure Fe_2O_3 (104) (-2.43 eV), the IpCOHP values between Fe1 and O1 on Mo-doped surfaces becomes less negative, indicating that the surface Fe-O bonding was weakened by the dopant Mo. This is consistent with the XPS

354 results of Mo 3d (Figure S6b). The lower binding energies of Mo 3d for Mo_x-Fe_2O_3 indicate the

355 deviation of the electron cloud from Fe^{3+} to Mo^{6+}, which is due to the strong electrophilicity of

356 Mo^{6+}, leading to the attenuation of the surface Fe-O bonding. Consequently, the neighboring

357 surface Fe site becomes more active. As displayed in the local density of states plot (Figure 3b),

358 when compared to pure Fe_2O_3 (104), the valence band of Fe1 site upshifts while the conduction

359 band of Fe1 site downshifts following introduction of Mo. This leads to the enhanced Lewis

360 acidity of the adjacent Fe site resulting from the introduction of Mo, as detected by *in situ* FTIR.

361 The adsorption energy of NH_3 at surface Fe1 site is increased from 0.69 eV on the pure Fe_2O_3

362 (104) surface to 1.15 eV with the dopant Mo at the surface (Figure 3c). However, the adsorption

363 of NH_3 on the clean surface Mo site at Mo-doped Fe_2O_3 (104) is only 0.56 eV (Figure S16). In

364 fact, introduction of the dopant with strong oxophilicity to the host metal oxide, improved the

365 Lewis acidity of the surface Fe sites. Thus, it is the parent ion rather than the dopant ion that are

366 the catalytically active sites, which is distinct from the traditional perspective on the active site in

367 doped oxide catalysts.[8,49] In addition, the high low-temperature activity originating from the

368 enhanced Lewis acidity is evidently different from the previous assumptions that Fe-based

369 oxides show high SCR activity due to the excellent redox property of Fe.[50-52]

370

13
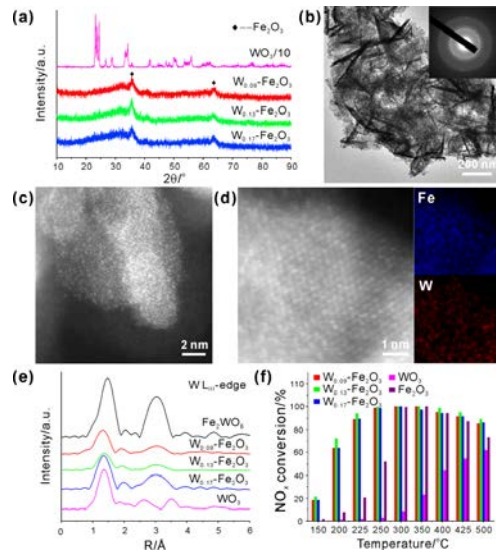
Figure 4. (a) XRD patterns of W_y-Fe$_2$O$_3$ catalysts, (b) TEM image and corresponding SAED pattern of W$_{0.13}$-Fe$_2$O$_3$, (c, d) HAADF images and EDS elemental mappings of W$_{0.25}$-Fe$_2$O$_3$, (e) RSF curves of W L$_{III}$-edge XAFS spectra for W_y-Fe$_2$O$_3$ and the reference samples, and (f) NO$_x$ conversions of Fe$_2$O$_3$ and W_y-Fe$_2$O$_3$ catalysts.

Following the above strategy, an alternative heteroatom, tungsten, which possesses similar characters to Mo, was doped into the Fe$_2$O$_3$ matrix. XRD patterns revealed weak signals (at 2θ ~ 30° and 60°) due to Fe$_2$O$_3$ with some broad features, suggesting low crystallinity of W_y-Fe$_2$O$_3$ (Figure 4a). TEM characterizations also indicate the absence of long-range ordered structure or serious distortion of the crystal structure (Figure 4b). HAADF-STEM shows large-scale disordered atoms arrangement (including Fe and W) in W$_{0.13}$-Fe$_2$O$_3$, and particularly, several bright flecks in the Fe$_2$O$_3$ microcrystal which are proposed as isolated W atoms (Figures 4c and

14

403   d), confirming an equivalent state of W as found for Mo. Furthermore, these dopant W ions are

404   highly dispersed throughout the whole Fe_2O_3 microcrystals as illustrated by EDS elemental

405   mappings (Figure 4d). XAFS shows that the hexavalent W atoms in W_y-Fe_2O_3 to possess the

406   same O_h coordination environment as that of Fe_2WO_6, and the lower intensity has been ascribed

407   to a distortion of the WO_6 octahedral structure (Figure 4e).[53] As predicted, the SCR activities of

408   W_y-Fe_2O_3 were clearly promoted especially at low temperatures (Figure 4f). This proof-of-

409   concept example confirmed that the partial substitution of Fe atoms by atomic-scale dopant

410   heteroatoms with octahedral coordination in the Fe_2O_3 lattice leads to the improved catalytic

411   performance.

412   **4. CONCLUSIONS**

413   Results here provide atomic-scale identification of catalytic active sites in Fe_2O_3-based oxide

414   catalysts with indiscernible microstructures. Detailed characterization combined with DFT

415   calculations confirmed that the catalytic active sites are not the dopant atoms themselves but

416   rather the adjacent Fe atoms whose electronic structure was modified by the dopant atoms

417   resulting in enhanced Lewis acidic properties of the catalyst. This new insight opens up a unique

418   perspective rgarding catalytic active sites in composite oxide catalysts with atomic-scale doping

419   used to maximize the efficiency of heteroatoms. This could be applied not only to this particular

420   reaction, but also to various other heterogeneous composite oxide catalytic systems.

421

422   ASSOCIATED CONTENT

15

Supporting Information. Catalytic performance tests, characterization methods, computational methods, and additional supplementary figures and tables. This material is available free of charge via the Internet at http://pubs.acs.org.

AUTHOR INFORMATION

Corresponding Author

*chm_zhangzl@ujn.edu.cn

*xmcao@ecust.edu.cn

*j.anderson@abdn.ac.uk

REFERENCES

(1) Piumetti, M.; Freyria, F. S.; Bonelli, B. *Chim. Oggi.* **2013**, 31, 55-58.

(2) Taylor, H. S. P. Roy. Soc. Lond. A Mat. **1925**, 108, 105-111.

(3) Jaramillo, T. F.; Jørgensen, K. P.; Bonde, J.; Nielsen, J. H.; Horch, S.; Chorkendorff, I. *Science* **2007**, 317, 100-102.

(4) Zambelli, T.; Wintterlin, J.; Trost, J.; Ertl, G. *Science* **1996**, 273, 1688-1690.

(5) Xie, X. W.; Li, Y.; Liu, Z. Q.; Haruta, M.; Shen, W. J. *Nature* **2009**, 458, 746-749.

450 (6) Cargnello, M.; Johnston-Peck, A. C.; Diroll, B. T.; Wong, E.; Datta, B.; Damodhar, D.;
451   Doan-Nguyen, V. V. T.; Herzing, A. A.; Kagan, C. R.; Murray, C. B. *Nature* **2015**, 524,
452   450-453.

453 (7) Wang, F.; Han, Y.; Lim, C. S.; Lu, Y. H.; Wang, J.; Xu, J.; Chen, H. Y.; Zhang, C.; Hong,
454   M. H.; Liu, X. G. *Nature* **2010**, 463, 1061-1065.

455 (8) McFarland, E. W.; Metiu, H. *Chem. Rev.* **2013**, 113, 4391-4427.

456 (9) Norris, D. J.; Efro, A. L.; Erwin, S. C. *Science* **2008**, 319, 1776-1779.

457 (10) Yang, Y. F.; Jin, Y. Z.; He, H. P.; Wang, Q. L.; Tao, Y.; Lu, H. M.; Ye, Z. Z. *J. Am. Chem.*
458   *Soc.* **2010**, 132, 13381-13394.

459 (11) Liang, X.; Wang, X.; Zhuang, Y.; Xu, B.; Kuang, S. M.; Li, Y. D. *J. Am. Chem. Soc.* **2008**,
460   130, 2736-2737.

461 (12) Smith, R. D. L.; Prévot, M. S.; Fagan, R. D.; Zhang, Z. P.; Sedach, P. A.; Siu, M. K. J.;
462   Trudel, S.; Berlinguette, C. P. *Science* **2013**, 340, 60-63.

463 (13) Shi, J. L. *Chem. Rev.* **2013**, 113, 2139-2181.

464 (14) Labinger, J. A. *Nature* **2016**, 536, 280-281.

465 (15) Wang, X. Q.; Rodriguez, J. A.; Hanson, J. C.; Gamarra, D.; Martínez-Arias, A.; Fernández-
466   García, M. *J. Phys. Chem. B* **2006**, 110, 428-434.

467 (16) Zhou, W.; Ross-Medgaarden, E. I.; Knowles, W. V.; Wong, M. S.; Wachs, I. E.; Kiely, C. J.
468   *Nat. Chem.* **2009**, 1, 722-728.

469 (17) Colussi, S.; Gayen, A.; Camellone, M. F.; Boaro, M.; Llorca, J.; Fabris, S.; Trovarelli, A.
470   *Angew. Chem. Int. Ed.* **2009**, 48, 8481-8484.

471 (18) Schaub, R.; Thorstrup, P.; Lopez, N.; Lægsgaard, E.; Stensgaard, I.; Nørskov, J. K.;
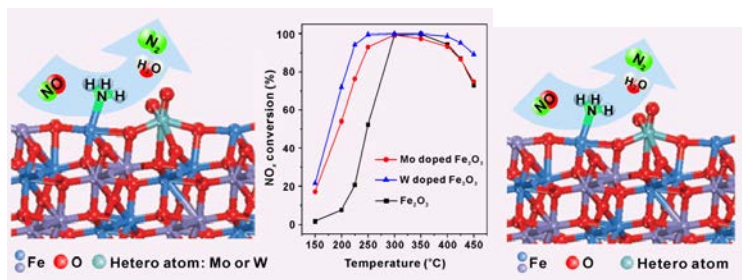472   Besenbacher, F. *Phys. Rev. Lett.* **2001**, 87, 266104.

473　(19) Qiao, B. T.; Wang, A. Q.; Yang, X. F.; Allard, L. F.; Jiang, Z.; Cui, Y. T.; Liu, J. Y.; Li, J.;

474　　　Zhang, T. *Nat. Chem.* **2011**, 3, 634-641.

475　(20) Jagadeesh, R. V.; Surkus, A.; Junge, H.; Pohl, M.; Radnik, J.;　Rabeah, J.; Huan, H.;

476　　　Schünemann, V.; Brückner, A.; Beller, M. *Science* **2013**, 342, 1073-1076.

477　(21) Busca, G.; Lietti, L.; Ramis, G.; Berti, F. *Appl. Catal. B* **1998**, 18, 1-36.

478　(22) Licht, S.; Cui, B. C.; Wang, B. H.; Li, F. F.; Lau, J.; Liu, S. Z. *Science* **2014**, 345, 637-640.

479　(23) Mou, X. L.; Zhang, B. S.; Li, Y.; Yao, L. D.; Wei, X. J.; Su, D. S.; Shen, W. J. *Angew.*

480　　　*Chem. Int. Ed.* **2012**, 51, 2989-2993.

481　(24) Lin, J.; Wang, A. Q.; Qiao, B. T.; Liu, X. Y.; Yang, X. F.; Wang, X. D.; Liang, J. X.; Li, J.;

482　　　Liu, J. Y.; Zhang, T. *J. Am. Chem. Soc.* **2013**, 135, 15314-15317.

483　(25) Li, Y.; Zhou, Y. X.; Ma, X.; Jiang, H. L. *Chem. Commun.* **2016**, 52, 4199-4202.

484　(26) Liu, F. D.; Yu, Y. B.; He, H. *Chem. Commun.* **2014**, 50, 8445-8463.

485　(27) Lietti, L.; Nova, I.; Ramis, G.; Acqua, L. D.; Busca, G.; Giamello, E.; Forzatti, P.; Bregani,

486　　　F. *J. Catal.* **1999**, 187, 419-435.

487　(28) Peng, Y.; Qu, R. Y.; Zhang, X. Y.; Li, J. H. *Chem. Commun.* **2013**, 49, 6215-6217.

488　(29) Liu, F. D.; He, H. *J. Phys. Chem. C* **2010**, 114, 16929-16936.

489　(30) Liu, F. D.; He, H.; Ding, Y.; Zhang, C. B. *Appl. Catal. B* **2009**, 93, 194-204.

490　(31) Zhu, H. B.; Rosenfeld, D. C.; Anjum, D. H.; Sangaru, S. S.; Saih, Y.; Ould-Chikh, S.; Basset,

491　　　J. *J. Catal.* **2015**, 329, 291-306.

492　(32) Li, P.; Xin, Y.; Li, Q.; Wang, Z. P.; Zhang, Z. L.; Zheng, L. R. *Environ. Sci. Technol.* **2012**,

493　　　46, 9600-9605.

494　(33) Bare, S. R.; Mitchell, G. E.; Maj, J. J.; Vrieland, G. E.; Gland, J. L. *J. Phys. Chem.* **1993**, 97,

495　　　6048-6053.

Deleted: <#>Backer, A. D.; Martinez, G. T.; Rosenauer, A.; Aert, S. V. *Ultramicroscopy* **2013**, *134*, 23.¶

498   (34)Brookes, C.; Wells, P. P.; Cibin, G.; Dimitratos, N.; Jones, W.; Morgan, D. J.; Bowker, M.

499   *ACS Catal.* **2014**, 4, 243-250.

500   (35)Gaur, A.; Shrivastava, B. D.; Joshi, S. K. *J. Phys.: Conf. Ser.* **2009**, 190, 012084.

501   (36)Yang, S. J.; Li, J. H.; Wang, C. Z.; Chen, J. H.; Ma, L.; Chang, H. Z.; Chen, L.; Peng, Y.;

502   Yan, N. Q. *Appl. Catal. B* **2012**, 117-118, 73-80.

503   (37)Chen, J. P.; Yang, R. T. *Appl. Catal. A* **1992**, 80, 135-148.

504   (38)Grasselli, R. K.; Sleight, A. W. Structure-activity and selectivity relationships in

505   heterogeneous catalysis, Elsevier, New York, **1991**.

506   (39)Long, R. Q.; Yang, R. T. *J. Catal.* **2002**, 207, 224-231.

507   (40)Li, Q.; Gu, H. C.; Li, P.; Fan, Y. Z.; Liu, Y.; Qi, Z. N.; Xin, Y.; Zhang, Z. L. *Chinese J.*

508   *Catal.* **2014**, 35, 1289-1298.

509   (41)Lin, S. D.; Gluhoi, A. C.; Nieuwenhuys, B. E. *Catal. Today* **2004**, 90, 3-14.

510   (42)Chen, L.; Li, J. H.; Ge, M. F. *Environ. Sci. Technol.* **2010**, 44, 9590-9596.

511   (43)Larrubia, M. A.; Ramis, G.; Busca, G. *Appl. Catal. B* **2000**, 27, L145-L151.

512   (44)Liu, Z. Q.; Millington, P. J.; Bailie, J. E.; Rajaram, R. R.; Anderson, J. A. *Micropor.*

513   *Mesopor. Mat.* **2007**, 104, 159-170.

514   (45)Kresse, G.; Furthmüller, J. *Phys. Rev. B* **1996**, 54, 11169-11186.

515   (46)Kresse, G.; Furthmüller, J. *Comp. Mater. Sci.* **1996**, 6, 15-50.

516   (47)Deringer, V. L.; Tchougreeff, A. L.; Dronskowski, R. *J. Phys. Chem. A* **2011**, 115, 5461-

517   5466.

518   (48)Maintz, S.; Deringer, V. L.; Tchougréeff, A. L.; Dronskowski, R. *J. Comput. Chem.* **2013**,

519   34, 2557-2567.

520   (49) Yang, X. F.; Wang, A. Q.; Qiao, B. T.; Li, J.; Liu, J. Y.; Zhang, T. *Accounts Chem. Res.*

521   **2013**, 46, 1740-1748.

522   (50) Liu, F. D.; He, H.; Zhang, C. B.; Shan, W. P.; Shi, X. Y. *Catal. Today* **2011**, 175, 18-25.

523   (51) Apostolescu, N.; Geiger, B.; Hizbullah, K.; Jan, M. T.; Kureti, S.; Reichert, D.; Schott, F.;

524   Weisweiler, W. *Appl. Catal. B* **2006**, 62, 104-114.

525   (52) Roy, S.; Viswanath, B.; Hegde, M. S.; Madras, G. *J. Phys. Chem. C* **2008**, 112, 6002-6012.

526   (53) Cavalcante, L. S.; Almeida, M. A. P.; Jr, W. A.; Tranquilin, R. L.; Longo, E.; Batista, N. C.;

527   Mastelaro, V. R.; Li, M. S. *Inorg. Chem.* **2012**, 51, 10675-10687.

528

529   **Table of Contents**

530

531